ICME impact at Earth with low and typical Mach number plasma characteristics

Antti Lakka[1], Tuija I. Pulkkinen[1], Andrew P. Dimmock[2], Emilia Kilpua[3], Matti Ala-Lahti[3],
Ilja Honkonen[4], Minna Palmroth[3], and Osku Raukunen[5]

[1]Department of Electronics and Nanoengineering, Aalto University, Finland
[2]Swedish Institute of Space Physics, Uppsala, Sweden
[3]Department of Physics, University of Helsinki, Helsinki, Finland
[4]Finnish Meteorological Institute, Helsinki, Finland
[5]Department of Physics and Astronomy, University of Turku, Turku, Finland

Correspondence: Antti Lakka (antti.lakka@aalto.fi)

Abstract.

We study how the the Earth's magnetosphere responds to the fluctuating solar wind conditions caused by two different amplitude interplanetary coronal mass ejection (ICME) events by using the Grand Unified Magnetosphere-Ionosphere Coupling Simulation (GUMICS-4). ICME events are known to drive strong geomagnetic disturbances and thus generate conditions that

5   may lead to saturation of the cross-polar cap potential (CPCP). The two ICME events occurred on 15–16 July 2012 and 29–30 April 2014. During the 2012 event, the solar wind upstream values reached up to 35 particles/cm^3, speed of 694 km/s, and interplanetary magnetic field of 22 nT. The event of 2014 was a moderate one, with the corresponding upstream values of 30 particles/cm^3, 320 km/s and 10 nT. The mean upstream Alfvén Mach number was 2.3 for the 2012 event, while it was 5.8 for the 2014 event. We examine how the Earth's space environment dynamics evolves during both ICME events covering both

10   global and local perspectives. To validate the accuracy of the GUMICS-4 simulation we use satellite data from several missions located in different parts of the magnetosphere. It is shown that the CPCP saturation is affected by the upstream conditions, with strong dependence on the Alfvén Mach number.

1   Introduction

According to the present understanding, the coupling of the solar wind and the Earth's magnetosphere is conducted by mag-

15   netic reconnection (Dungey, 1961) and viscous processes (Axford and Hines, 1961) such as the Kelvin-Helmholtz instability (e.g. Nykyri and Otto (2001)) and diffusion (Johnson and Cheng, 1997). Although viscous processes may play a strong role, particularly when the interplanetary magnetic field (IMF) is directed northward (IMF $B_Z > 0\,\mathrm{nT}$) (e.g. Osmane et al. (2015)), magnetic reconnection on the dayside magnetopause is responsible for the majority of plasma transport during southward interplanetary magnetic field IMF (IMF $B_Z < 0\,\mathrm{nT}$), which is also when the solar wind couples to the Earth's space environment

20   more efficiently (Nishida, 1968; Koustov et al., 2009). The intervals of extended periods of strongly southward IMF typically arise when the Earth is hit by an interplanetary coronal mass ejection (ICME) (see e.g. Kilpua et al. (2017b)). ICMEs are

interplanetary counterparts of coronal mass ejections (CMEs), gigantic eruptions of plasma and magnetic field from the Sun, and it is now firmly established that ICMEs also drive the strongest geomagnetic disturbances (e.g., Gosling et al. (1991); Huttunen et al. (2002); Richardson and Cane (2012); Kilpua et al. (2017a)). The signatures of ICMEs at 1 AU have been debated since their first observational evidence: High helium abundance (Hirshberg et al., 1972), high magnetic field magnitude and

5   low plasma beta (Hirshberg and Colburn, 1969; Burlaga et al., 1981), low ion temperatures (Gosling et al., 1973), and smooth rotation of the magnetic field Burlaga et al. (1981). While there have been attempts to form a universal set of signatures to describe ICMEs (Gosling, 1990; Richardson and Cane, 2003), they vary significantly such that no single set of criteria are able to describe all the ICME events, and none of them are unique to ICMEs. For example, only one third to one half of all the ICMEs have a magnetic flux rope (or a magnetic cloud) (e.g. Gosling, 1990; Richardson and Cane, 2003), whose signatures

10 combine enhanced magnetic field, reduced proton temperature, and the smooth rotation of the magnetic field over an interval of a day (Burlaga et al., 1981). While magnetic clouds are the most studied part of ICMEs due to their significant potential to cause large space weather storms, their relationship to the entire ICME sequence still pose many questions (e.g., Kilpua et al. (2013)). Moreover, if the ICME is sufficiently faster than the surrounding solar wind plasma, a shock is formed ahead of the ICME (Goldstein et al., 1998), with a region of compressed solar wind plasma between the leading shock front and the

15 magnetic cloud, that is referred to as the sheath.

The two regions, sheath and ejecta, are the most distinctive parts of ICMEs (see e.g. Kilpua et al. (2017b)), which both can drive intense magnetic storms (e.g. Tsurutani et al. (1988); Huttunen and Koskinen (2004)). Sheaths and ejecta, however, have clear differences in their solar wind conditions and consequently differences in the solar wind - magnetosphere coupling (Jianpeng et al., 2010; Pulkkinen et al., 2007; Kilpua et al., 2017b). The reasons behind this different response is currently not

20 fully understood. ICME sheaths typically include high solar wind dynamic pressure and fluctuating IMF direction, with both northward and southward orientations occurring within a short time period (Kilpua et al., 2017b). The duration of the sheath is also typically shorter than the following cloud, for example in their study Zhang et al. (2012) obtained the average values of 10.6 and 30.6 hours for sheaths and clouds, respectively. Sheaths are known to enhance high-latitude ionospheric currents (Huttunen and Koskinen, 2004), and they are found to have higher coupling efficiency than clouds (Yermolaev et al., 2012).

25 The clouds typically enhance the equatorial ring current (Huttunen and Koskinen, 2004).

Due to potential for strongly southward IMF orientation ICME magnetic clouds provide periods of the enhanced magnetospheric activity. Moreover, during cloud events due to the combination of generally high magnetic fields and low plasma densities, the solar wind Alfvén Mach number M_A can reach quite low values and even close to unity. The role of M_A for solar wind - magnetosphere coupling has been highlighted in recent studies (Lavraud and Borovsky, 2008; Lopez et al., 2010;

30 Myllys et al., 2016, 2017). In particular, the role low M_A conditions typical to ICME magnetic cloud for the saturation of the ionospheric cross-polar cap potential has been a subject of several studies(e.g. Ridley, 2005, 2007; Lopez et al., 2010; Wilder et al., 2015; Myllys et al., 2016; Lakka et al., 2018).

Global MHD models have been extensively used to study the effects of ICMEs on the magnetospheric and ionospheric dynamics. A recent paper by Kubota et al. (2017) studied the Bastille Day geomagnetic storm event (July 15, 2000) driven by a

35 halo CME that erupted from the Sun on July 14. They found that the inclusion of auroral conductivity in the ionospheric part

of the global MHD model by Tanaka (1994) led to the saturated CPCP without any effect on the field-aligned currents, thus suggesting a current system with a dynamo in the magnetosphere and a load in the ionosphere.

In this study we use GUMICS-4 (Janhunen et al., 2012), the global MHD simulation, and consider two ICME events, one being significantly stronger in terms of the solar wind driver. The comparisons include the subsolar magnetopause position, the amount of energy transferred from the solar wind into the magnetosphere, the CPCP, and the magnetic field magnitude within the inner part of the magnetosphere. We pay special attention to the magnetic clouds within the ICMEs by using two different spatial resolutions.

This paper is structured in a following way: Section 2 describes GUMICS-4 global MHD code, characteristics of the two ICME events, and the executed simulations, Section 4 presents the main results from global and local perspectives, followed by discussion and conclusions.

2 Methodology

2.1 GUMICS-4 Global MHD Simulation

The simulations in this study were executed using the fourth edition of the Grand-Unified Magnetosphere-Ionosphere Coupling Simulation (GUMICS-4), in which a 3D MHD magnetosphere is coupled with a spherical electrostatic ionosphere (Janhunen et al., 2012). The finite volume MHD solver solves the ideal MHD equations with the separation of the magnetic field to a curl-free (dipole) component and divergent-free component created by currents external to the Earth ($\mathbf{B} = \mathbf{B_0} + \mathbf{B_1}(t)$) (Tanaka, 1994). The MHD simulation box has dimensions of 32 ... -224 R_E in X_{GSE} direcion and -64 ... +64 R_E in both Y_{GSE} and Z_{GSE} directions, while the inner boundary is spherical with a radius of 3.7 R_E. In order to make the computations feasible on a single processor, GUMICS-4 uses temporal subcycling and adaptive cartesian octogrid. The former reduces the number of MHD computations an order of magnitude while maintaining the local Courant-Friedrichs-Levy (CFL) constraint (J.L. Lions, 2000, p. 121 — 151). The latter ensures that whenever there are large gradients, the grid is refined thus resolving smaller-scale features especially close to boundaries and current sheets.

The ionospheric grid is triangular and densest in the auroral oval while in the polar caps the grid is still rather dense, with about 180 km and 360 km spacing used in the two regions, respectively. The ionosphere is driven by field-aligned currents, and electron precipitation from the magnetosphere, as well as by solar EUV ionisation. Field-aligned currents contribute to the cross-polar cap potential through

$$\nabla \cdot \mathbf{J} = \nabla \cdot \left[\Sigma \cdot \left(-\nabla \phi + V_n \times \mathbf{B} \right) \right] = -j_{||} \left(\hat{\mathbf{b}} \cdot \hat{\mathbf{r}} \right), \tag{1}$$

where $\mathbf{J}$ is current density, Σ is the height-integrated conductivity tensor, ϕ is the ionospheric potential, V_n the neutral wind caused by the Earth's rotation, $j_{||}$ is the field-aligned current, and $\left(\hat{\mathbf{b}} \cdot \hat{\mathbf{r}} \right)$ is the cosine of the angle between the magnetic field direction $\hat{\mathbf{b}}$ and the radial direction $\hat{\mathbf{r}}$ (Janhunen et al., 2012). Electron precipitation and solar EUV ionisation have contributions on the height-integrated Pedersen and Hall conductivities with solar EUV ionisation parametrized by the 10.7 cm solar radio flux that has a numerical value of 100×10^{-22} W/m^2. Electron precipitation affects the ionospheric electron densities, which

are calculated at different altitudes and are used when computing the height-integrated Pedersen and Hall conductivities. The details on the ionsopheric part of GUMICS-4 can be found in Janhunen and Huuskonen (1993).

The region between the MHD magnetosphere and the electrostatic spherical ionosphere is a passive medium where no currents flow perpendicular to the magnetic field. The magnetosphere is coupled to the ionosphere using dipole mapping of the field-
5 aligned current pattern and the electron precipitation from the magnetosphere to the ionosphere and the electric potential from the ionosphere to the magnetosphere. This feedback loop is updated every 4 seconds.

2.2 GUMICS simulations of two ICME events

We use both 0.5 and 0.25 R_E maximum spatial resolutions as well as varying dipole tilt angle in this study. Two complete ICME periods were simulated using 0.5 R_E resolution by starting with nominal solar wind conditions preceding the events,
10 and ending with nominal conditions following the events. To give GUMICS-4 magnetosphere time to form Lakka et al. (2017), the simulations were initialized with two hours of constant solar wind driving using upstream values equal to those used during the first minute of the actual simulation.

Due computational limitations, using the best maximum spatial resolution (0.25 R_E) covering both ICME events with full length is not feasible. Hence two additional runs were performed with 0.25 R_E maximum spatial resolution in order to gain
15 a more detailed view of the dynamics of the magnetosphere and ionosphere when the ICME magnetic cloud was propagating past the Earth. These runs lasted 6 hours each, and were executed by restarting the 0.5 R_E runs with enhanced resolution. Table 1 summarizes all four simulation runs related to the study.

3 Observations of two ICME events

We retrieve the solar wind data from the NASA OMNIWeb service (http://omniweb.gsfc.nasa.gov) and the solar energetic
20 particle data from the NOAA NCEI Space Weather data access (https://www.ngdc.noaa.gov/stp/satellite/goes/index.html) for the two ICME events studied here. Onset times for the ICME sheath (i.e., the shock time) and the magnetic cloud boundary times are retrieved from the Wind spacecraft ICME catalogue (https://wind.nasa.gov/ICMEindex.php). Figures 1 and 2 show the upstream parameters during both events. For both figures IMF X, Y, Z components and the IMF magnitude are shown in panel a, upstream plasma flow velocity X, Y, Z components in panel b, the upstream plasma number density in panel c,
25 upstream Alfvén Mach number in panel d, energetic proton fluxes for three GOES-15 energy channels between 8–80 MeV in panel e, and the cross-polar cap potential from the GUMICS-4 simulation in panel f. Figure 1 includes time range from 09:00 UT, July 14 to 15:00 UT, July 17, 2012, while Figure 2 shows the period from 19:00 UT, April 28 to 17:00 UT, May 1, 2014. The time of the ICME shock, and the start and end times of the ICME are marked with vertical red lines in both figures. The gray-shaded regions indicate the time periods simulated with the maximal 0.25 R_E spatial resolution. Both IMF and plasma
30 flow velocity components are given in GSE coordinate system.

Figure 1 shows the arrival of the leading shock at 18:53 UT on July 14, 2012 as the simultaneous abrupt jump in the plasma and magnetic field parameters and the following ICME sheath as irregular directional changes of the IMF and compressed plasma

and field. The energetic particle fluxes for the two lower energy channels increase until after the shock passage, which suggests continual particle acceleration in the shock driven by the ICME. At 06:54 UT on July 15, the onset of the ICME magnetic cloud is identified by the turning of the IMF orientation to strongly southward, the number density reducing significantly and the clear decrease in the variability of the magnetic field. During the next 45 hours the IMF direction stays strongly southward

5 and it rotates slowly towards less southward orientation. We note that in the trailing part of the ICME the field changes rather sharply to northward orientation and there continues to rotated to south. We cannot rule out that this end part is not another small ICME, but as our study focuses on the strong southward magnetic fields in the main part of the ICME we do not consider the origin of this end part further here.

The ICME on April 2014 was slower than the July 2012 ICME and its speed is very close to the ambient solar wind speed.

10 Hence, no shock, nor clear sheath developed ahead of this ICME. The onset of the ICME related disturbance is marked by the increased plasma number density followed by a rapid decrease and a clear southward turning of the IMF at 20.38 UT on April 29 (Figure 2). The lack of shock is also supported by the lack of energetic particle fluxes above background. The very beginning of this cloud may contain some disturbed preceding solar wind (the region of higher density and fluctuating field), but we do not separate it in this study as a sheath and focus our study on the effects of the cloud part.

15 Both magnetic clouds are featured with low Alfvén Mach number. In the 2012 case M_A falls even below unity and is 1.9 on average during the cloud structure, while during the 2014 magnetic cloud the minimum M_A was 3.8 and 5.8 on average.

The 2012 event features generally larger CPCP, with its values residing above 40 kV, increasing gradually and reaching 70 kV (Figure 1f). Opposite to this, the CPCP peaks early to reach 50 kV during the 2014 event and subsequently reduces to 20 kV (Figure 2f).

20 The 2012 ICME is considerably longer than the 2014 event, with 57 hours 26 minutes total duration, of which 12 hours 1 minute are sheath, and 45 hours 25 minutes belong to the magnetic cloud. The 2014 event lasted 21 hours 13 minutes in total. The 2012 ICME had larger effects on magnetospheric dynamics, as the solar wind driving was considerably stronger, with the average IMF magnitude and solar wind speed of 14 nT and 490 km/s, respectively, compared with 8.5 nT and 303 km/s of the 2014 event. The maximum IMF magnitude and upstream solar wind speed were also larger during the 2012 event, with

25 21 (10) nT and 660 (321) km/s maximum values measured during the 2012 (2014) cloud. However, while maximum number density was higher during the 2012 magnetic cloud (36 cm^{-3} vs. 30 cm^{-3}), the average number density was considerably higher during the 2014 event (2012: 2 cm^{-3} vs. 2014: 12 cm^{-3}).

During the two ICME events, data from the Cluster 1 (hereafter Cluster) and Geotail satellites were available from the CDAWeb service (https://cdaweb.sci.gsfc.nasa.gov/index.html/). Figure 3 shows the orbits of Cluster (blue) and Geotail (magenta) along

30 with the magnetopause location (black) from the empirical Shue model Shue et al. (1997) on the XY plane (figures 3a and 3c) and on the XZ plane (figures 3b and 3d) during both events. Magnetopause position is computed for the most earthward magnetopause location during the events. Note that the orbit tracks include intervals of nominal upstream conditions before and after the ICME events. Starting points and ending points of the time intervals under inspections are marked with a cross and a triangle, respectively. Dots mark the (located visually) points where satellite orbits intersect the magnetopause. It should

35 be noted that since the magnetopause position is not stable, but rather in motion during the events, the intersection points are

only approximations. The used coordinate system is GSE. Based on figure 3, the Cluster spacecraft orbits inside of the magnetosphere throughout the 2012 event and most of the 2014 event. On the other hand, Geotail is outside of the magnetosphere an extended period during July 16-17, 2012. as well as during April 28, late April 30, and early May 1 in 2014.

Figures 4 and 5 show time series of the magnetic field magnitude $|B|$ along the Geotail (panel a) and Cluster (panel b) orbits

5   during the 2012 and 2014 events. Magenta (Geotail) and blue (Cluster) curves show the actual in-situ data, while the black curve shows the magnetic field magnitude along the spacecraft orbits in GUMICS-4 simulation. The gray-shaded regions in panels a and b show when the respective spacecraft is outside the magnetosphere according to Figure 3. Note that logarithmic scale is used for the Cluster data. Panel c in both figures shows the radial distance of both spacecraft from the center of the Earth.

10   At the start of the 2012 event, Geotail resides in the plasma sheet, but quickly moves to the boundary layer (roughly July 14, 16:00 UT to July 15, 06:00 UT), after which it enters the lobe as the cloud proper hits the magnetosphere. At around the time of the end of the data gap towards the end of July 16, the spacecraft moves to the low latitude boundary layer and the magnetosheath (supported by the plasma data not shown here).

At the start of the 2012 event, Cluster is near perigee recording field values close to those of the dipole. Cluster exits the ring

15   current region around 16:00 UT on July 14, and enters the plasma sheet. A brief encounter in the lobe is recorded between roughly 18:00 UT July 15 and 06:00 July 16. A second period in the inner magnetosphere commences around 12:00 UT on July 16, with exit to the lobe after 00:00 UT July 17 (supported by the plasma and energetic particle data not shown here).

4 Analysis

4.1 Global dynamics

20   Figures 6 and 7 show the effect of upstream IMF B_Z (panel a), and solar wind dynamic pressure (panel b) on the magnetopause nose (panel c), total energy through the dayside magnetopause (panel d) and the ionospheric cross-polar cap potential CPCP (panel e) during the 6 hour intervals run in higher resolution (gray shading in figures 1 and 2. The $0.5\,\mathrm{R_E}$ resolution run results are shown in black, and $0.25\,\mathrm{R_E}$ resolution results are shown in magenta. We identify the magnetopause nose position from the maximum value of J_Y along the Sun-Earth line at one-minute temporal resolution, smoothed using 10-min sliding averages.

25   This value is compared with the Shue (Shue et al., 1997) empirical magnetopause model. Total energy through the dayside magnetopause is computed by evaluating the Poynting flux in the vicinity of the (Shue) magnetopause, and its component parallel to the magnetopause surface normal. These values are integrated over the surface of the magnetopause Sunward of the terminator.

Figure 6c shows that during the first four hours of the 6-hour run the magnetopause position predictions (black and magenta

30   curves) by GUMICS-4 are close to the Shue et al. (1997) model (blue curve). During the last 2 hours, however, there are more fluctuations in the GUMICS-4 magnetopause position, especially in the $0.5\,\mathrm{R_E}$ resolution run. From July 15, 21:00 UT to July 16, 01:00 UT the simulation runs agree on the magnetopause location and also with the Shue model, with differences within 10% all the time of the first 4 hours. However, the last two hours show more variations between the three curves: The finest

resolution show slight outward motion of the magnetopause, which toward the end of the period is less than that predicted by the Shue model. On the other hand, the 0.5 R_E resolution run shows inward indentations followed by outward motion consistent with the Shue model. Overall, the 0.5 R_E resolution run is 58% of the time within 10% of the Shue model, and the 0.25 R_E resolution run agree 67% of the time within 10% of the Shue model. Over the entire periods, the 0.25 R_E run is within

5   10% of the Shue model 92% of the time, while the 0.5 R_E run reaches within 10% 89% of the time.

After the increase of the IMF B_Z from -16 nT to -14 nT during the first hour, hours from 22 to 01 feature steady IMF B_Z and slightly fluctuating solar wind dynamic pressure (figures 6a-6b), while the last 2 hours the conditions change, with IMF B_Z increasing gradually and the dynamic pressure dropping below 0.5 nPa. In these conditions, the Shue model predicts the magnetopause nose to move sunward, as does GUMICS-4, albeit the accuracy of the predictions depends on the used

10   resolution.

The higher-resolution run yielded better agreement with the magnetopause location, because increasing the spatial resolution sharpens the gradients and allows better identification of the location of the maxima (Janhunen et al., 2012). Comparison of the runs shows, however, that the results are consistent with each other, indicating that the lower-resolution run is providing similar large-scale dynamics as the finer-resolution run.

15   Differences between the simulations in local measures, such as the magnetopause nose position, do not show in global variables, such as the total energy through the dayside magnetopause surface. As can be seen from Figure 6d, the curves of the two different spatial resolution runs are almost identical. This emphasizes the interpretation that integrated quantities, such as energy, which give a better representation of the true physical properties of the magnetosphere in the GUMICS-4 solution, are not dependent on grid resolution (Janhunen et al., 2012). We acknowledge that using more sophisticated methods for

20   computing the magnetopause surface could potentially lead to more accurate results. The Shue model was however used since it is relatively easy to apply and also because most of the large-scale variations with respect to the measurements occur in the nightside magnetopause, which is neglected in this study. In addition, our results are mostly of the same order of magnitude compared to what was obtained by Palmroth et al. (2003) by using plasma flow streamlines for computing the magnetopause surface from GUMICS-4 results.

25   The magnetosphere – ionosphere coupling, however, here illustrated by the CPCP time evolution in Figure 6e demonstrates differences between the 0.25 R_E and the 0.5 R_E runs, with the higher resolution run producing 20-30% higher CPCP than the lower resolution run during the first three hours after the 0.25 R_E run has stabilized, which happens within 10 minutes after July 15, 21:00 UT. During the last 3 hours, the CPCP predicted by the 0.5 R_E run increases significantly to almost reach the high-resolution run cross-polar cap potential. This coincides with the time when the magnetopause has moved further away

30   from the Earth in the simulations. The expansion of the magnetosphere is also verified by the Shue model.

The time evolution of the magnetopause position in Figure 7 is similar regardless of the used spatial resolution, with both simulation runs responding similarly to small upstream fluctuations. Both simulation runs stay within 10% of the Shue model prediction for the entire 6-hour period. As in the case of the 2012 event, the two simulation runs are almost inseparable in terms of the incoming solar wind energy (Figure 7d). However, while the 2012 and 2014 events are similar also in terms of higher

CPCP in the fine resolution simulation (up to 250% in the 2014 event), CPCP is quite stable in the 2014 event in both low and high resolution throughout the 6 hour interval.

4.2 Saturation of the Cross-polar cap Potential

Figures 8 and 9 show the CPCP (both northern and southern hemispheres are considered) as a function of the solar wind electric field E_Y component for both ICME events. Color-coding marks the IMF magnitude in figures 8a and 9a, solar wind speed in figures 8b and 9b, and the upstream Alfvén Mach number in figures 8c and 9c. Every data point in Figure 8 (9) is computed from 10-minute averages, binned by E_Y with 1.0 (0.5) mV/m intervals. The ICME sheath (solid circles) and cloud (solid squares) periods as well as the nominal solar wind conditions (solid triangles) prior to and following the events are analyzed separately. Note that here only the coarse grid (0.5 R_E) simulation results are used, as we analyze the effects during the entire magnetic cloud and sheath periods including times before and after the event not covered by the high-resolution run.

Figure 8 shows that the response of the CPCP to the upstream E_Y is quite linear during the magnetic cloud (squares) when solar wind driving electric field E_Y is below 5 mV/m, during nominal solar wind conditions (triangles), and ICME sheath (tilted squares). However, the polar cap potential first decreases and subsequently saturates during the cloud when the solar wind driving is stronger ($E_Y > 5$ mV/m). For the 2012 event, we refer to the E_Y range from 0 to 5 mV/m as the linear regime, and from 5 mV/m upward as the non-linear regime.

Figure 8a shows the obvious result that highest E_Y values are associated with highest IMF magnitudes. However, it also shows that the largest IMF magnitudes are associated with the non-linear regime, indicating that strong upstream driving leads to the CPCP saturation. In addition, Figure 8b suggests that the increase of the CPCP in the linear regime is clearly higher for lower velocity values (cloud structure), than for higher velocity values (sheath and nominal conditions). Generally, this agrees with the previous studies utilizing statistical (Newell et al., 2008) and numerical (Lopez et al., 2010) tools. The latter authors suggest that this is caused by the solar wind flow diversion in the pressure gradient-dominated magnetosheath; faster solar wind will produce more rapid diversion of the flow around the magnetosphere, and thus smaller amount of plasma will reach the magnetic reconnection site.

Figure 8c shows that the upstream Alfvén Mach number M_A is at or above 4 ($M_A \geq 4$) during the nominal solar wind conditions and during the ICME sheath, while during the magnetic cloud M_A resided below 4 and almost reaches unity. This supports the interpretation that saturation of the CPCP depends on the upstream Alfvén Mach number M_A such that saturation occurs only when M_A values fall below 4. The dependence of the CPCP saturation on M_A is well-known, documented both in measurements (Wilder et al., 2011; Myllys et al., 2016) and in simulation studies (Lopez et al., 2010; Lakka et al., 2018).

Figure 9 seems to agree with the view presented above, as the response of the CPCP to the upstream E_Y during the 2014 event is quite linear regardless of IMF magnitude (Figure 9a), plasma flow speed (Figure 9b), or the large-scale solar wind driving structure (ICME cloud or nominal solar wind), which however do not vary very much during the event. This is apparently because solar wind driving is substantially weaker during the 2014 event than during the 2012 event, with IMF magnitude reaching barely 10 nT, and upstream plasma flow speed varying only order of 10 km/s. As a result, the upstream Alfvén Mach number $M_A > 4$ throughout the ICME event as well as during the nominal solar wind conditions. The high polar cap potential

values for the lowest E_Y bin is associated with the large density enhancement driving polar cap potential increase before the arrival of the cloud proper.

Figure 10 shows the region 1 and region 2 field-aligned current (FAC) system as an indicator of the coupling of the magnetosphere and the ionosphere (e.g. Siscoe et al. (1991)). The four panels show how field-aligned currents are distributed in the
5   northern hemisphere ionosphere in July 16, 2012 at 01:00 UT and 03:00 UT at 0.5 R_E maximum resolution (figures 10a–10b) and at 0.25 R_E maximum resolution (figures 10c–10d). Current density is shown both as color coding and contours, while the white dotted line depicts the polar cap boundary.

4.3 Local dynamics

Figures 4 and 5 show the time series of the IMF magnitude $|B|$ in the Geotail and Cluster orbits during the 2012 and 2014
10   events compared with the GUMICS-4 results along the satellite tracks. Overall, GUMICS-4 underestimates $|B|$ measured by both satellites, but the time evolution of the magnetic field is generally similar.

Prior to the arrival of the sheath region in the 2012 event, Geotail enters the plasma sheet boundary layer earlier than predicted by GUMICS-4. During the sheath there are many dips and peaks in both plots, with the difference between measured (both Geotail and Cluster) and predicted values varying, as can be seen from figures 4a and 4b. Also, Figure 4a shows that starting
15   from July 17, 00:00 UT the in-situ value in Geotail orbit increases as the satellite goes to the magnetosheath proper, while GUMICS-4 prediction decreases as the orbit track in GUMICS-4 approaches the shock region (see Figure 3a). The 2014 event shows similar features especially when Geotail enters and exits the magnetosphere at 23:14 UT, April 28, and at 12:00 UT, April 30, respectively, with measured (by Geotail) $|B|$ in the former case fluctuating and rising sharply from 10 nT to 40 nT while the predicted $|B|$ increases more steadily from a few nT to 20 nT as the satellite enters from the magnetosheath to the
20   magnetosphere. In the latter case decrease (increase) of measured (simulated) $|B|$ occurs several hours after the spacecraft exits the magnetosphere (later grey-shaded region in Figure 5a) possibly because of the inaccuracies in defining the moment of exit. Note that while Cluster makes an entry into the magnetosphere at 16:12 UT, April 29, GUMICS-4 predicts a position within the magnetosheath and an entry into the magnetosphere only following the end of the cloud.

Note that the Cluster perigee (2 R_E) (Figure 4c) is below the inner boundary of the GUMICS-4 simulation (3.7 R_E), which
25   causes the simulation field to record unphysical values around the time of the maximas at 09:00 on July 14, 2012 and 15:00 on July 16, 2012, and hence there are data gaps in GUMICS-4 data plots.

The effect of the ICME sheath is visible after the onset of the sheath in Figure 4, with both measured and predicted $|B|$ fluctuating. The ICME magnetic cloud proper seems to cause largest difference in $|B|$ during the 2012 event, when the driving was quite strong.

30   ## 5 Discussion

In this paper we study how the magnetosphere responds to two ICME events with different characteristics by means of using the GUMICS-4 global MHD simulation. The 2012 event was stronger in terms of solar wind driver, the 2014 event being

significantly weaker both in terms of solar wind speed and IMF magnitude. We considered both global and local parameters, including magnetopause nose position along the Sun-Earth -line, total energy transferred from the solar wind into the magnetosphere, and the ionospheric cross-polar cap potential (CPCP). Local measures include response of the magnetic field magnitude along the orbits of Cluster and Geotail spacecraft. The two ICME events were simulated using 0.5 R_E maximum

5 spatial resolution. To test the effect of grid resolution enhancement on global dynamics, we simulated 6 hour subsets of both CME cloud periods with 0.25 R_E maximum spatial resolution.

The magnetopause location changes in response to solar wind driving in the GUMICS-4 results is dependent on the driver intensity: Stronger driving during the 2012 CME magnetic cloud leads to larger differences as compared to the (Shue et al., 1997) model, whereas the agreement between the simulation and the empirical model is quite good during weaker driving

10 during the 2014 event (figures 6 and 7). Comparison of the magnetopause location between the 0.25 R_E (0.5 R_E) resolution run and the Shue model show that the relative difference between the two is below 10% 92% (89%) of the 6 hour subset in 2012 (Figure 6), while corresponding analysis of the 6 hour subset in 2014 (Figure 7) yielded differences below 10% 100% of the time regardless of the resolution.

When the solar wind density and pressure decrease during 01:00-03:00 UT, July 16, 2012 leading to expansion of the magneto-

15 sphere, the difference between the Shue model predictions and GUMICS-4 results grows, with 0.25 (0.5) R_E maximum spatial resolution resulting in 67% (58%) within 10% of the Shue model. In comparison, GUMICS-4 results for both resolution runs during the first four hours (July 15, 21:00 UT – July 16, 01:00 UT) were within 10%. It is thus apparent that using coarse grid (0.5 R_E) leads to larger difference in magnetopause nose position than using fine grid (0.25 R_E), if the solar wind density is very low, and the overall driving is relatively strong.

20 When spatial resolution is increased, gradient quantities such as J_Y have sharper profiles and therefore larger values Janhunen et al. (2012). As it is the maximum value of J_Y that we use to locate the magnetopause nose, the nose position evaluation in the lower resolution runs is more ambiguous both due to the larger spread of the current and due to the larger grid cell size. This may lead to changes in the maximum value up to several R_E over short time periods in response to upstream fluctuations. In the finer resolution runs, J_Y distribution is sharper, which leads to lesser fluctuations in the maximum value determination.

25 However, the differences between the two grid resolutions occur only under rapidly varying solar wind or very low solar wind density conditions.

The empirical models developed by Shue et al. Shue et al. (1997, 1998) are based on statistical analysis of large number of spacecraft measurements of plasma and magnetic field during magnetopause crossings. While the Shue et al. (1997) model is optimized for moderate upstream conditions, the Shue et al. (1998) targets especially stronger driving periods. However, we

30 computed the difference in the magnetopause position between the two models and found that it is mostly less than 0.1 R_E with maximum difference of 0.4 R_E, with Shue et al. (1997) model predicting more sunward magnetopause nose. Because of the small difference at the magnetopause nose, we have only used Shue et al. (1997) model in our study.

Differences in the magnetopause location do not necessarily translate into differences in global measures, as can be seen from figures 6d and 7d, which show the time evolution of the energy transferred from the solar wind through the magnetopause

35 surface. The response of the total energy E_{tot} during both ICME cloud periods is quite similar regardless of the used grid

resolution. As an integrated quantity, energy entry is a better indicator of the true physical processes of GUMICS-4 solution and does not suffer from dependence on grid resolution like the maximum J_Y (Janhunen et al., 2012). Therefore, in analyses of simulation results, it would be better to consider such global integrated quantities, even if they have no direct observational counterparts.

5   In the ionosphere, the cross-polar cap potential value is dependent on the grid resolution, with higher resolution yielding higher polar cap potential values. However, typically, the time evolution is similar for both resolutions. As can be seen in Figure 6e, the difference between the two resolution runs can be up to 30% during the first 4 hours of the 6 hour stage, until the CPCP obtained from the 0.5 R_E resolution run starts to increase and eventually catches the 0.25 R_E resolution run at 03:00 UT. Similar evolution is absent during the 2012 event (Figure 7e). Thus, at least two factors contribute to the ionospheric coupling:

10   Grid resolution and intensity of solar wind driving.

The polar cap structure and the distribution of the FAC do not change much in either of the simulations, thus suggesting that the coupling of the magnetosphere and the ionosphere remains relatively constant. As is shown in figures 10a–10b, the region 1 currents are clearly visible, while the region 2 currents get stronger only by enhancing the grid resolution in the MHD region Janhunen et al. (2012). However, the upstream conditions change considerably from 01:00 to 03:00, with the upstream Alfvén

15   Mach number decreasing from 1.9 to 0.6, suggesting that polar cap potential saturation mechanisms is likely to take place (Ridley, 2007; Wilder et al., 2015; Lakka et al., 2018). We therefore conclude that the increase of the CPCP during the 0.5 R_E simulation run is caused by processes outside of the magnetosphere, likely in the magnetosheath, and that GUMICS-4 responds differently to low Alfvén Mach number solar wind depending on grid resolution.

Figures 8 and 9 illustrate the CPCP as a function of the solar wind E_Y component. Color-coded are the IMF magnitude

20   in figures 8a and 9a, the solar wind speed in figures 8b and 9b, and the upstream Alfvén Mach number in figures 8c and 9c. Nominal solar wind conditions before and after the actual ICME events as well as the ICME sheath and cloud periods are considered separately. We note that only results from the maximum spatial resolution (0.25 R_E) runs are included in the figures. Consistent with earlier studies, Figure 8 shows saturation of the CPCP during high solar wind driving (see e.g. Shepherd (2007); Russell et al. (2001)): With nominal solar wind conditions or during ICME sheath period the response of the CPCP to

25   the upstream E_Y is rather linear, while for ICME cloud period the CPCP saturates, when $E_Y > 5\mathrm{mV/m}$. From Figure 8a it can be seen that the saturation occurs when $B > 12\,\mathrm{nT}$ and Figure 8b shows that the increase of the CPCP in the linear regime depends on the upstream velocity in such a way that the increase is clearly higher for lower velocity values (cloud event), than for higher velocity values (sheath event and nominal conditions), as suggested by previous statistical (Newell et al., 2008) and numerical (Lopez et al., 2010) studies. The latter study proposes that this is because of the more rapid diversion of the solar

30   wind flow in the pressure gradient dominated magnetosheath under faster solar wind, which leaves a smaller amount of plasma at the magnetic reconnection site.

The saturation of the CPCP is absent in Figure 9 due to the significantly weaker solar wind driving during the 2014 event (the upstream E_Y is below 4 $\mathrm{mV/m}$). This in turn leads to the upstream Alfvén Mach number to be on average 5.8 during the ICME cloud event. Lavraud and Borovsky (2008) suggests that when the Alfvén Mach number decreases below 4 and

35   the overall magnetosheath plasma beta (p/p_B, where p is the plasma pressure and p_B the magnetic pressure) below 1, the

magnetosheath force balance changes such that plasma flow streamlines are diverted away from the magnetic reconnection merging region in the dayside magnetopause (Lopez et al., 2010), which causes the CPCP saturation. However, the CPCP saturation limit of $M_A = 4$ is not necessarily the only governing parameter, as there is both observational evidence with large M_A values (up to 7.3) (Myllys et al., 2016) and simulation results indicating saturation at low but above $M_A = 1$ values (this

5   study). Nonetheless, our results suggest that the saturation of the CPCP is dependent on the upstream M_A in such a way that M_A needs to be below 4 for the saturation to occur.

An interesting aspect is that the CPCP does not reach its maximum simultaneously with E_Y, i.e. the CPCP is largest with moderate E_Y (5–6 mV/m) (see Figure 8). As E_Y increases to 11 mV/m, the CPCP decreases from 70 kV to 40 kV. This is actually apparent in Figure 1h as well: The absolute values of both B_Z and V_X reach their maximum values a few hours

10   after the onset of the magnetic cloud, which is at 6.54 UT, July 15. However, the CPCP is at that time quite moderate, about 40 kV, and does not reach its maximum until July 16, when both B_Z and V_X have already reduced significantly. Thus the CPCP overshoots in Figure 8, a feature that was not observed in a GUMICS-4 study by Lakka et al. (2018) using artificial solar wind input consisting of relatively high density and constant driving parameters.

The performance of GUMICS-4 was put to test by means of comparing the magnetic field magnitude $|B|$ to in-situ data of

15   Cluster and Geotail satellites. We conclude that ICME cloud period leads to largest differences in $|B|$ between measured and in-situ data especially during high solar wind driving. Furthermore, during high driving, the magnetopause location estimates may not be sufficiently accurate to cause differences in the observed satellite position and GUMICS-4 prediction within/outside the magnetosphere.

6   Conclusions

20   The results of this paper can be summarized as follows:

(1) Enhancing spatial resolution of the magnetosphere in GUMICS-4 affects the accuracy of the determination of the the magnetopause subsolar point. Some global measures, such as energy transferred from the solar wind into the magnetosphere, are not affected. However, the cross-polar cap potential can be affected significantly, with up to over factor of 2 difference between simulations using different spatial resolutions for the magnetosphere.

25   (2) Our results show signs of cross-polar cap potential saturation during low upstream Alfvén Mach number thus agreeing with previous studies.

(3) Overall time evolution of the magnetic field magnitude $|B|$ observed by Cluster and Geotail is similar to that predicted by GUMICS-4, although GUMICS-4 generally overestimates the field magnitude. The largest differences emerge during the ICME magnetic cloud, when the solar wind driving is particularly strong.

30   *Data availability.* Solar wind data are freely available from the NASA/GSFC Omniweb server (https://omniweb.gsfc.nasa.gov/). Solar energetic particle data are freely available from the NOAA NCEI Space Weather data access (https://www.ngdc.noaa.gov/stp/satellite/goes/index.html).

Competing interests. The authors declare that they have no conflict of interest.

Acknowledgements. The calculations presented above were performed using computer resources within the Aalto University School of Science "Science-IT" project. This project was funded by the Academy of Finland grants #1267087, #288472, and #310444. We acknowledge use of NASA/GSFC's Space Physics Data Facility's OMNIWeb service, and OMNI data. Solar energetic particle data supplied courtesy of

5 ngdc.noaa.gov.

References

Axford, W. I. and Hines, C. O.: A UNIFYING THEORY OF HIGH-LATITUDE GEOPHYSICAL PHENOMENA AND GEOMAGNETIC STORMS, Canadian Journal of Physics, 39, 1433–1464, https://doi.org/10.1139/p61-172, http://dx.doi.org/10.1139/p61-172, 1961.

Burlaga, L., Sittler, E., Mariani, F., , and Schwenn, R.: Magnetic loop behind an interplanetary shock: Voyager, Helios, and IMP 8 observations, Journal of Geophysical Research: Space Physics, 86, 6673–6684, https://doi.org/10.1029/JA086iA08p06673, https://agupubs.onlinelibrary.wiley.com/doi/abs/10.1029/JA086iA08p06673, 1981.

Dungey, J. W.: Interplanetary Magnetic Field and the Auroral Zones, Phys. Rev. Lett., 6, 47–48, https://doi.org/10.1103/PhysRevLett.6.47, http://link.aps.org/doi/10.1103/PhysRevLett.6.47, 1961.

Goldstein, R., Neugebauer, M., and Clay, D.: A statistical study of coronal mass ejection plasma flows, Journal of Geophysical Research: Space Physics, 103, 4761–4766, https://doi.org/10.1029/97JA03663, https://agupubs.onlinelibrary.wiley.com/doi/abs/10.1029/97JA03663, 1998.

Gosling, J. T.: Coronal Mass Ejections and Magnetic Flux Ropes in Interplanetary Space, pp. 343–364, American Geophysical Union (AGU), https://doi.org/10.1029/GM058p0343, https://agupubs.onlinelibrary.wiley.com/doi/abs/10.1029/GM058p0343, 1990.

Gosling, J. T., Pizzo, V., and Bam, S. J.: Anomalously low proton temperatures in the solar wind following interplanetary shock waves—evidence for magnetic bottles?, Journal of Geophysical Research, 78, 2001–2009, https://doi.org/10.1029/JA078i013p02001, https://agupubs.onlinelibrary.wiley.com/doi/abs/10.1029/JA078i013p02001, 1973.

Gosling, J. T., McComas, D. J., Phillips, J. L., and Bame, S. J.: Geomagnetic activity associated with earth passage of interplanetary shock disturbances and coronal mass ejections, Journal of Geophysical Research: Space Physics, 96, 7831–7839, https://doi.org/10.1029/91JA00316, https://agupubs.onlinelibrary.wiley.com/doi/abs/10.1029/91JA00316, 1991.

Hirshberg, J. and Colburn, D. S.: Interplanetary field and geomagnetic variations—a unifield view, Planetary and Space Science, 17, 1183 – 1206, https://doi.org/https://doi.org/10.1016/0032-0633(69)90010-5, 1969.

Hirshberg, J., Bame, S. J., and Robbins, D. E.: Solar flares and solar wind helium enrichments: July 1965-July 1967, Solar Physics, 23, 467–486, https://doi.org/10.1007/BF00148109, https://doi.org/10.1007/BF00148109, 1972.

Huttunen, K. E. J. and Koskinen, H. E. J.: Importance of post-shock streams and sheath region as drivers of intense magnetospheric storms and high-latitude activity, Annales Geophysicae, 22, 1729–1738, https://hal.archives-ouvertes.fr/hal-00317357, 2004.

Huttunen, K. E. J., Koskinen, H. E. J., and Schwenn, R.: Variability of magnetospheric storms driven by different solar wind perturbations, Journal of Geophysical Research: Space Physics, 107, SMP 20–1–SMP 20–8, 2002.

Janhunen, P. and Huuskonen, A.: A numerical ionosphere-magnetosphere coupling model with variable conductivities, Journal of Geophysical Research: Space Physics, 98, 9519–9530, https://doi.org/10.1029/92JA02973, http://dx.doi.org/10.1029/92JA02973, 1993.

Janhunen, P., Palmroth, M., Laitinen, T., Honkonen, I., Juusola, L., Facskó, G., and Pulkkinen, T.: The GUMICS-4 global {MHD} magnetosphere–ionosphere coupling simulation, Journal of Atmospheric and Solar-Terrestrial Physics, 80, 48 – 59, https://doi.org/http://dx.doi.org/10.1016/j.jastp.2012.03.006, http://www.sciencedirect.com/science/article/pii/S1364682612000909, 2012.

Jianpeng, G., Xueshang, F., Jie, Z., Pingbing, Z., and Changqing, X.: Statistical properties and geoefficiency of interplanetary coronal mass ejections and their sheaths during intense geomagnetic storms, Journal of Geophysical Research: Space Physics, 115, https://doi.org/10.1029/2009JA015140, https://agupubs.onlinelibrary.wiley.com/doi/abs/10.1029/2009JA015140, 2010.

J.L. Lions, G. C.: Handbook of Numerical Analysis. Solution of Equations in Rn (Part 3), Techniques of Scientific Computing (Part 3), vol. Volume 7, North-Holland, 1 edn., 2000.

Johnson, J. R. and Cheng, C. Z.: Kinetic Alfvén waves and plasma transport at the magnetopause, Geophysical Research Letters, 24, 1423–1426, https://doi.org/10.1029/97GL01333, http://dx.doi.org/10.1029/97GL01333, 1997.

5 Kilpua, E., Isavnin, A., Vourlidas, A., Koskinen, H., and Rodriguez, L.: On the relationship between interplanetary coronal mass ejections and magnetic clouds, 31, 1251–1265, 2013.

Kilpua, E., Koskinen, H. E. J., and Pulkkinen, T. I.: Coronal mass ejections and their sheath regions in interplanetary space, Living Reviews in Solar Physics, 14, 5, https://doi.org/10.1007/s41116-017-0009-6, https://doi.org/10.1007/s41116-017-0009-6, 2017a.

Kilpua, E. K. J., Balogh, A., von Steiger, R., and Liu, Y. D.: Geoeffective Properties of Solar Transients and Stream Interaction Regions, Space
10   Science Reviews, 212, 1271–1314, https://doi.org/10.1007/s11214-017-0411-3, https://doi.org/10.1007/s11214-017-0411-3, 2017b.

Koustov, A. V., Khachikjan, G. Y., Makarevich, R. A., and Bryant, C.: On the SuperDARN cross polar cap potential saturation effect, Annales Geophysicae, 27, 3755–3764, https://doi.org/10.5194/angeo-27-3755-2009, 2009.

Kubota, Y., Nagatsuma, T., Den, M., Tanaka, T., and Fujita, S.: Polar cap potential saturation during the Bastille Day storm event using global MHD simulation, Journal of Geophysical Research: Space Physics, 122, 4398–4409, https://doi.org/10.1002/2016JA023851, http:
15   //dx.doi.org/10.1002/2016JA023851, 2016JA023851, 2017.

Lakka, A., Pulkkinen, T. I., Dimmock, A. P., Osmane, A., Honkonen, I., Palmroth, M., and Janhunen, P.: The impact on global mag-netohydrodynamic simulations from varying initialisation methods: results from GUMICS-4, Annales Geophysicae, 35, 907–922, https://doi.org/10.5194/angeo-35-907-2017, https://www.ann-geophys.net/35/907/2017/, 2017.

Lakka, A., Pulkkinen, T. I., Dimmock, A. P., Myllys, M., Honkonen, I., and Palmroth, M.: The Cross-Polar Cap Saturation in GUMICS-
20   4 During High Solar Wind Driving, Journal of Geophysical Research: Space Physics, 0, https://doi.org/10.1002/2017JA025054, https://agupubs.onlinelibrary.wiley.com/doi/abs/10.1002/2017JA025054, 2018.

Lavraud, B. and Borovsky, J. E.: Altered solar wind-magnetosphere interaction at low Mach numbers: Coronal mass ejections, Journal of Geophysical Research: Space Physics, 113, n/a–n/a, https://doi.org/10.1029/2008JA013192, http://dx.doi.org/10.1029/2008JA013192, a00B08, 2008.

25 Lopez, R. E., Bruntz, R., Mitchell, E. J., Wiltberger, M., Lyon, J. G., and Merkin, V. G.: Role of magnetosheath force balance in regulating the dayside reconnection potential, Journal of Geophysical Research: Space Physics, 115, n/a–n/a, https://doi.org/10.1029/2009JA014597, http://dx.doi.org/10.1029/2009JA014597, a12216, 2010.

Myllys, M., Kilpua, E., Lavraud, B., and Pulkkinen, T. I.: Solar wind-magnetosphere coupling efficiency during ejecta and sheath-driven geomagnetic storms, p. 4378–4396, https://doi.org/10.1002/2016JA022407, http://urn.fi/URN:NBN:fi:aalto-201610124801, 2016.

30 Myllys, M., Kipua, E. K. J., and Lavraud, B.: Interplay of solar wind parameters and physical mechanisms producing the saturation of the cross polar cap potential, Geophysical Research Letters, 44, 3019–3027, https://doi.org/10.1002/2017GL072676, https://agupubs.onlinelibrary.wiley.com/doi/abs/10.1002/2017GL072676, 2017.

Newell, P. T., Sotirelis, T., Liou, K., and Rich, F. J.: Pairs of solar wind-magnetosphere coupling functions: Combining a merging term with a viscous term works best, Journal of Geophysical Research: Space Physics, 113, n/a–n/a, https://doi.org/10.1029/2007JA012825,
35   http://dx.doi.org/10.1029/2007JA012825, a04218, 2008.

Nishida, A.: Coherence of geomagnetic DP 2 fluctuations with interplanetary magnetic variations, Journal of Geophysical Research, 73, 5549–5559, https://doi.org/10.1029/JA073i017p05549, http://dx.doi.org/10.1029/JA073i017p05549, 1968.

Nykyri, K. and Otto, A.: Plasma transport at the magnetospheric boundary due to reconnection in Kelvin-Helmholtz vortices, Geophysical Research Letters, 28, 3565–3568, https://doi.org/10.1029/2001GL013239, http://dx.doi.org/10.1029/2001GL013239, 2001.

Osmane, A., Dimmock, A., Naderpour, R., Pulkkinen, T., and Nykyri, K.: The impact of solar wind ULF B-z fluctuations on geomagnetic activity for viscous timescales during strongly northward and southward IMF, JOURNAL OF GEOPHYSICAL RESEARCH: SPACE PHYSICS, 120, 9307–9322, https://doi.org/10.1002/2015JA021505, 2015.

Palmroth, M., Pulkkinen, T. I., Janhunen, P., and Wu, C.-C.: Stormtime energy transfer in global MHD simulation, Journal of Geophysical Research: Space Physics, 108, n/a–n/a, https://doi.org/10.1029/2002JA009446, http://dx.doi.org/10.1029/2002JA009446, 1048, 2003.

Pulkkinen, T. I., Partamies, N., Huttunen, K. E. J., Reeves, G. D., and Koskinen, H. E. J.: Differences in geomagnetic storms driven by magnetic clouds and ICME sheath regions, Geophysical Research Letters, 34, https://doi.org/10.1029/2006GL027775, https://agupubs. onlinelibrary.wiley.com/doi/abs/10.1029/2006GL027775, 2007.

Richardson, I. G. and Cane, H. V.: Identification of interplanetary coronal mass ejections at 1 AU using multiple solar wind plasma composition anomalies, Journal of Geophysical Research: Space Physics, 109, https://doi.org/10.1029/2004JA010598, https://agupubs. onlinelibrary.wiley.com/doi/abs/10.1029/2004JA010598, 2003.

Richardson, I. G. and Cane, H. V.: Solar wind drivers of geomagnetic storms during more than four solar cycles, J. Space Weather Space Clim., 2, A01, https://doi.org/10.1051/swsc/2012001, https://doi.org/10.1051/swsc/2012001, 2012.

Ridley, A. J.: A new formulation for the ionospheric cross polar cap potential including saturation effects, Annales Geophysicae, 23, 3533–3547, https://hal.archives-ouvertes.fr/hal-00318077, 2005.

Ridley, A. J.: Alfvén wings at Earth's magnetosphere under strong interplanetary magnetic fields, Annales Geophysicae, 25, 533–542, https://doi.org/10.5194/angeo-25-533-2007, http://www.ann-geophys.net/25/533/2007/, 2007.

Russell, C. T., Luhmann, J. G., and Lu, G.: Nonlinear response of the polar ionosphere to large values of the interplanetary electric field, Journal of Geophysical Research: Space Physics, 106, 18 495–18 504, https://doi.org/10.1029/2001JA900053, http://dx.doi.org/10.1029/2001JA900053, 2001.

Shepherd, S. G.: Polar cap potential saturation: Observations, theory, and modeling, Journal of Atmospheric and Solar-Terrestrial Physics, 69, 234–248, 2007.

Shue, J.-H., Chao, J. K., Fu, H. C., Russell, C. T., Song, P., Khurana, K. K., and Singer, H. J.: A new functional form to study the solar wind control of the magnetopause size and shape, Journal of Geophysical Research: Space Physics, 102, 9497–9511, https://doi.org/10.1029/97JA00196, http://dx.doi.org/10.1029/97JA00196, 1997.

Shue, J.-H., Song, P., Russell, C. T., Steinberg, J. T., Chao, J. K., Kokubun, S., Singer, H. J., Detman, T. R., Zastenker, G., Vaisberg, O. L., and Kawano, H.: Magnetopause location under extreme solar wind conditions, Journal of Geophysical Research: Space Physics, 103, 17 691–17 700, https://doi.org/10.1029/98JA01103, https://agupubs.onlinelibrary.wiley.com/doi/abs/10.1029/98JA01103, 1998.

Siscoe, G. L., Lotko, W., and Sonnerup, B. U.: A high-latitude, low-latitude boundary layer model of the convection current system, Journal of Geophysical Research: Space Physics, 96, 3487–3495, 1991.

Tanaka, T.: Finite Volume TVD Scheme on an Unstructured Grid System for Three-Dimensional MHD Simulation of Inhomogeneous Systems Including Strong Background Potential Fields, Journal of Computational Physics, 111, 381 – 389, https://doi.org/http://dx.doi.org/10.1006/jcph.1994.1071, http://www.sciencedirect.com/science/article/pii/S0021999184710710, 1994.

Tsurutani, B. T., Gonzalez, W. D., Tang, F., Akasofu, S. I., and Smith, E. J.: Origin of interplanetary southward magnetic fields responsible for major magnetic storms near solar maximum (1978–1979), Journal of Geophysical Research: Space Physics, 93, 8519–8531, https://doi.org/10.1029/JA093iA08p08519, https://agupubs.onlinelibrary.wiley.com/doi/abs/10.1029/JA093iA08p08519, 1988.

Wilder, F. D., Clauer, C. R., Baker, J. B. H., Cousins, E. P., and Hairston, M. R.: The nonlinear response of the polar cap potential under southward IMF: A statistical view, Journal of Geophysical Research: Space Physics, 116, n/a–n/a, https://doi.org/10.1029/2011JA016924, http://dx.doi.org/10.1029/2011JA016924, a12229, 2011.

Wilder, F. D., Eriksson, S., and Wiltberger, M.: The role of magnetic flux tube deformation and magnetosheath plasma beta in the saturation of the Region 1 field-aligned current system, Journal of Geophysical Research: Space Physics, 120, 2036–2051, https://doi.org/10.1002/2014JA020533, http://dx.doi.org/10.1002/2014JA020533, 2014JA020533, 2015.

Yermolaev, Y. I., Nikolaeva, N. S., Lodkina, I. G., and Yermolaev, M. Y.: Geoeffectiveness and efficiency of CIR, sheath, and ICME in generation of magnetic storms, Journal of Geophysical Research: Space Physics, 117, https://doi.org/10.1029/2011JA017139, https://agupubs.onlinelibrary.wiley.com/doi/abs/10.1029/2011JA017139, 2012.

Zhang, J., Poomvises, W., and Richardson, I. G.: Sizes and relative geoeffectiveness of interplanetary coronal mass ejections and the preceding shock sheaths during intense storms in 1996–2005, Geophysical Research Letters, 35, https://doi.org/10.1029/2007GL032045, https://agupubs.onlinelibrary.wiley.com/doi/abs/10.1029/2007GL032045, 2012.

Table 1. Summary of the event simulations within the current study.

Event year	Nominal solar wind [h]	Event date and time	Event length [h]	Resolution [R_E]
2012	9.9	18:53 UT, July 14 – 04:19 UT, July 17	57.4	0.5
2014	25.6	20:38 UT, April 29 – 17:51 UT, April 30	21.2	0.5
2012	0	21:00 UT, July 15 – 03:00 UT, July 16	6	0.25
2014	0	00:00 UT, April 30 – 06:00 UT, April 30	6	0.25
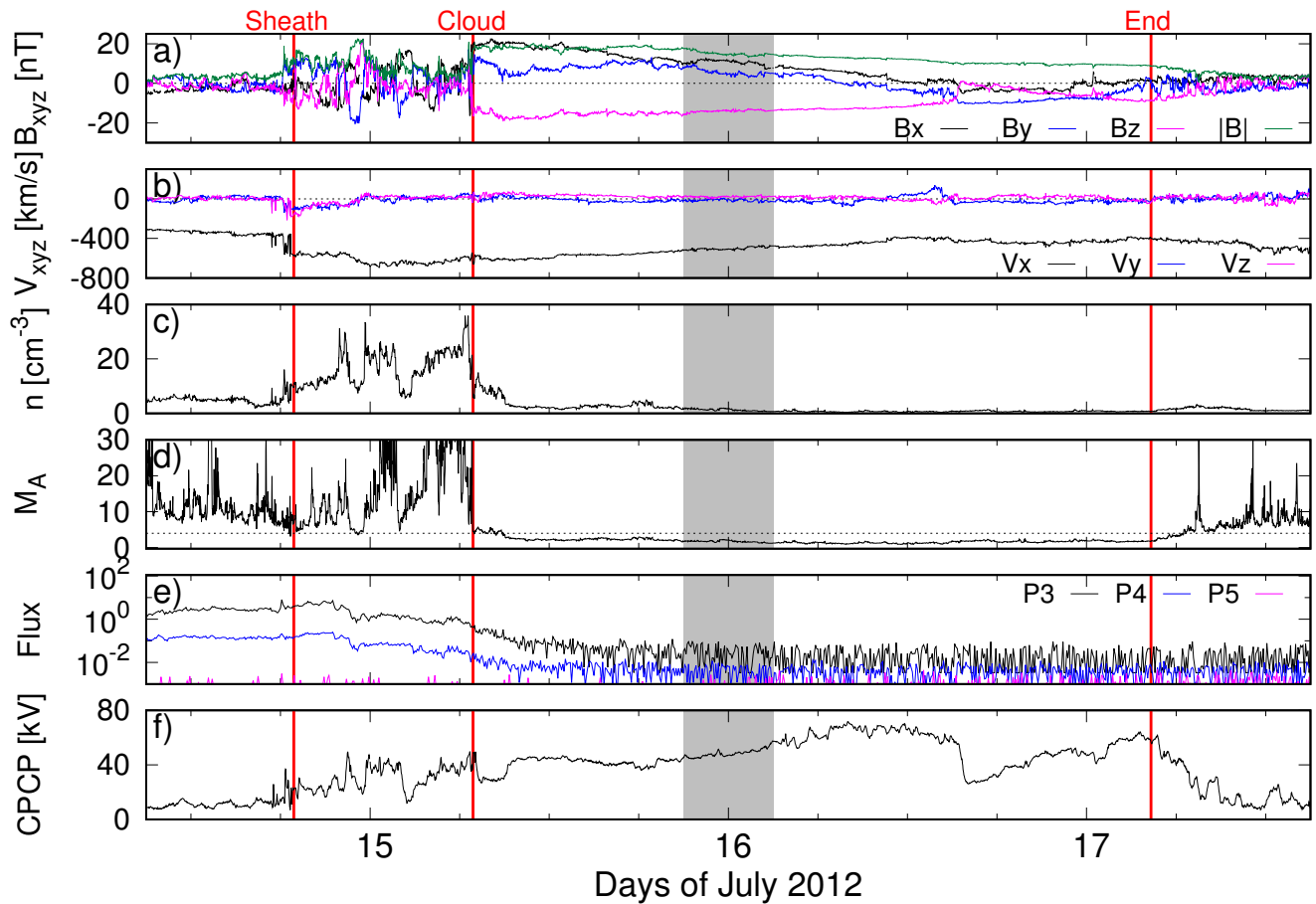
Figure 1. Solar wind and IMF conditions during July 14 09:00 UT – July 17 15:00 UT, 2012. Panels from top to bottom: a) IMF components B_X, B_Y and B_Z and the IMF magnitude in nT, b) plasma velocity components V_X, V_Y and V_Z in km/s, c) plasma number density n in cm^{-3}, d) upstream Alfvén Mach number M_A ($M_A = 4$ is marked with dotted line), e) proton fluxes for three energy channels between 8–80 MeV, and f) the cross-polar cap potential from GUMICS-4. Vertical red lines indicate onset of the ICME sheath/magnetic cloud or the end of the ICME event. Grey background shows which part of the ICME event is simulated using both 0.25 and 0.5 R$_E$ as a maximum spatial resolution.
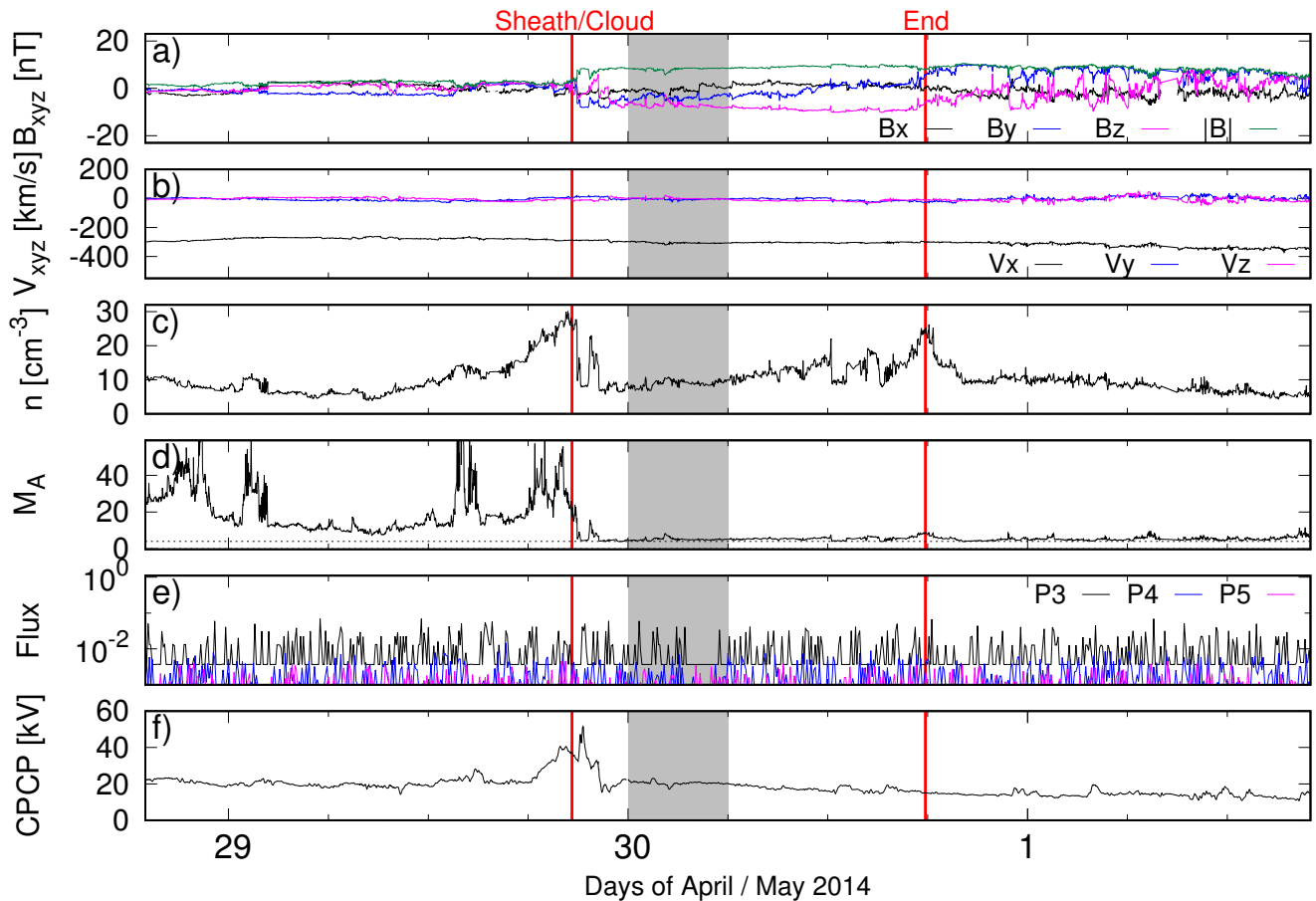
Figure 2. Solar wind and IMF conditions during April 28 19:00 UT – May 1 17:00 UT, 2014. Panels from top to bottom: a) IMF components B_X, B_Y and B_Z and the IMF magntiude in nT, b) plasma velocity components V_X, V_Y and V_Z in km/s, c) plasma number density n in cm^{-3}, d) upstream Alfvén Mach number M_A ($M_A = 4$ is marked with dotted line), e) proton fluxes for three energy channels between 8–80 MeV, and f) the cross-polar cap potential from GUMICS-4. Vertical red lines indicate onset of the ICME sheath/magnetic cloud or the end of the ICME event. Grey background shows which part of the ICME event is simulated using both 0.25 and 0.5 $\mathrm{R_E}$ as a maximum spatial resolution.
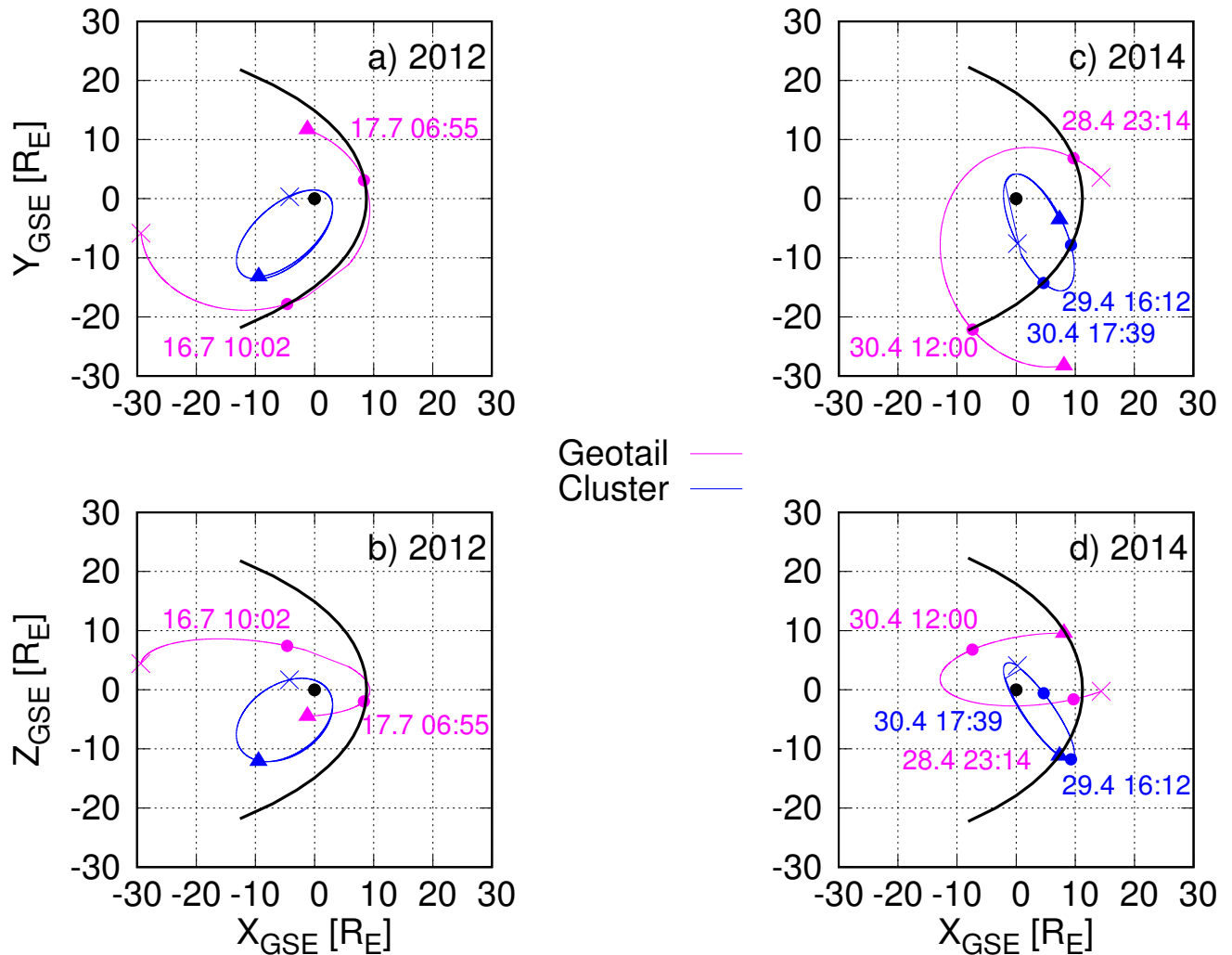
Figure 3. Orbits of Cluster 1 (blue) and Geotail (magenta) satellites during July 14 09:00 UT – July 17 15:00 UT, 2012 (panels a and b) and during April 28 19:00 UT – May 1 17:00 UT, 2014 (panels c and d). Orbits are shown on the XY plane in panels a and c and on the XZ plane in panels b and d. The used coordinate system is GSE. The most earthward occurrence of the Shue magnetopause during both time intervals is drawn with black. Starting and ending points of the time intervals under inspections are marked with a cross and a triangle, respectively, while the approximate points where satellite orbits intersect the magnetopause are marked with dots.
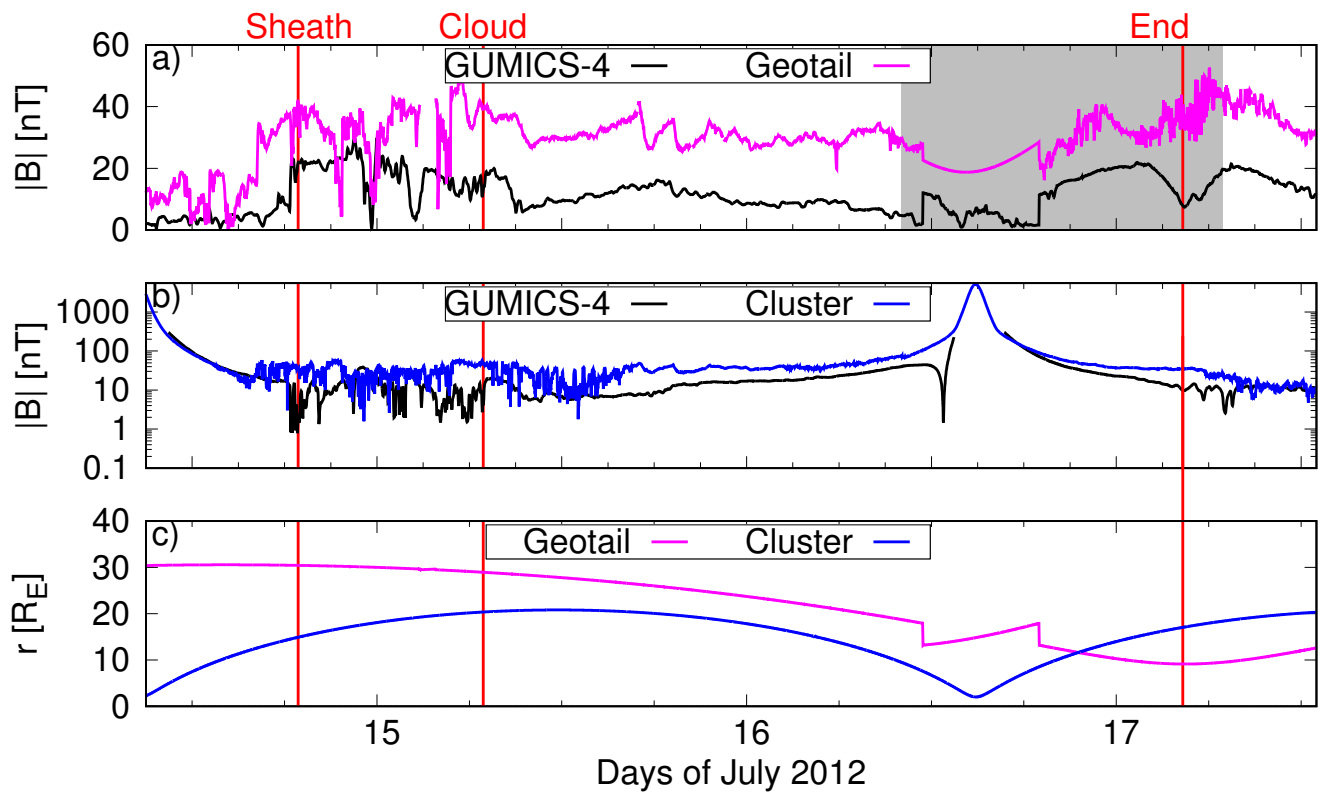
Figure 4. The time series of the magnetic field magnitude $|B|$ along the orbits of Geotail (panel a) and Cluster 1 (panel b) during July 14 09:00 UT – July 17 15:00 UT, 2012 measured by the two satellites (Geotail as magenta and Cluster 1 as blue) and predicted by GUMICS-4 (black). Panel c: Radial distance of both spacecraft from the center of the Earth. Grey-shaded regions indicate approximate time intervals when satellite is outside the magnetosphere.
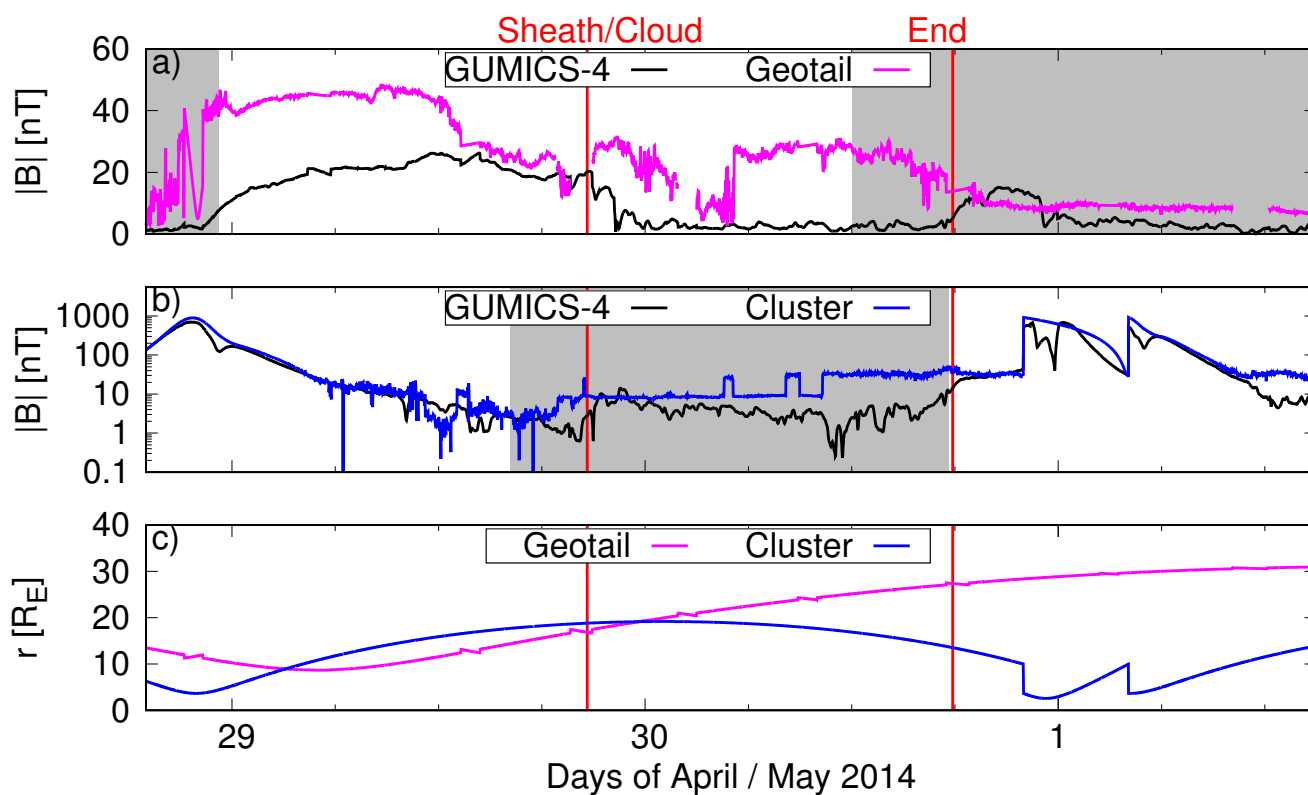
Figure 5. The time series of the magnetic field magnitude $|B|$ along the orbits of Geotail (panel a) and Cluster 1 (panel b) during April 28 19:00 UT – May 1 17:00 UT, 2014 measured by the two satellites (Geotail as magenta and Cluster 1 as blue) and predicted by GUMICS-4 (black). Panel c: Radial distance of both spacecraft from the center of the Earth. Grey-shaded regions indicate approximate time intervals when satellite is outside the magnetosphere.
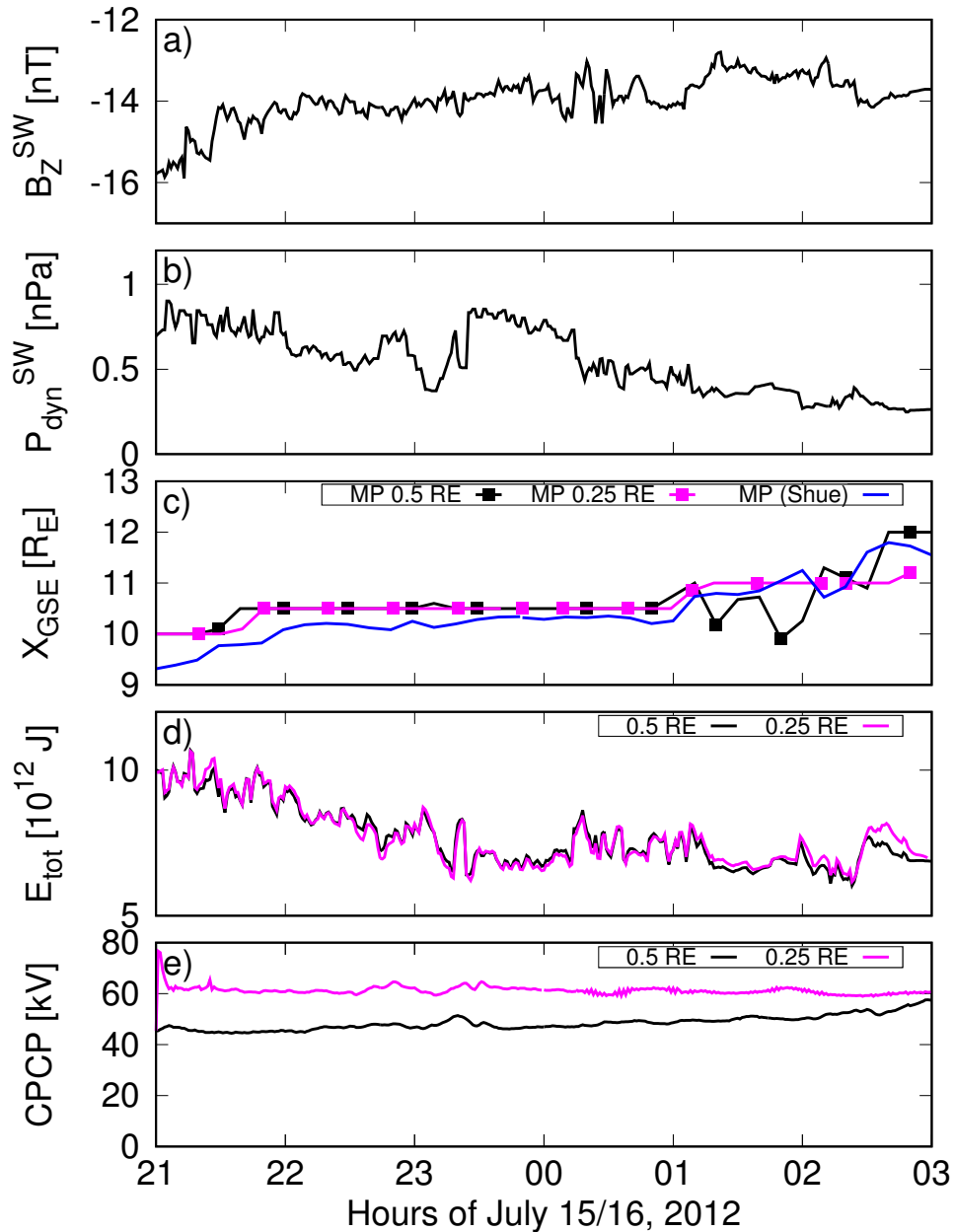
Figure 6. a) Interplanetary magnetic field z component, b) solar wind dynamic pressure, c) the nose of the magnetopause, d) energy transferred from the solar wind into the magnetosphere through the dayside magnetopause, and e) the cross-polar cap potential during July 15 21:00 UT - July 16 03:00 UT, 2012. Black and magenta plots in panels c–d imply which maximum spatial resolution is used (0.5 (black) and 0.25 (magenta) R_E). Blue plot in panel c marks the magnetopause nose computed using the Shue model.
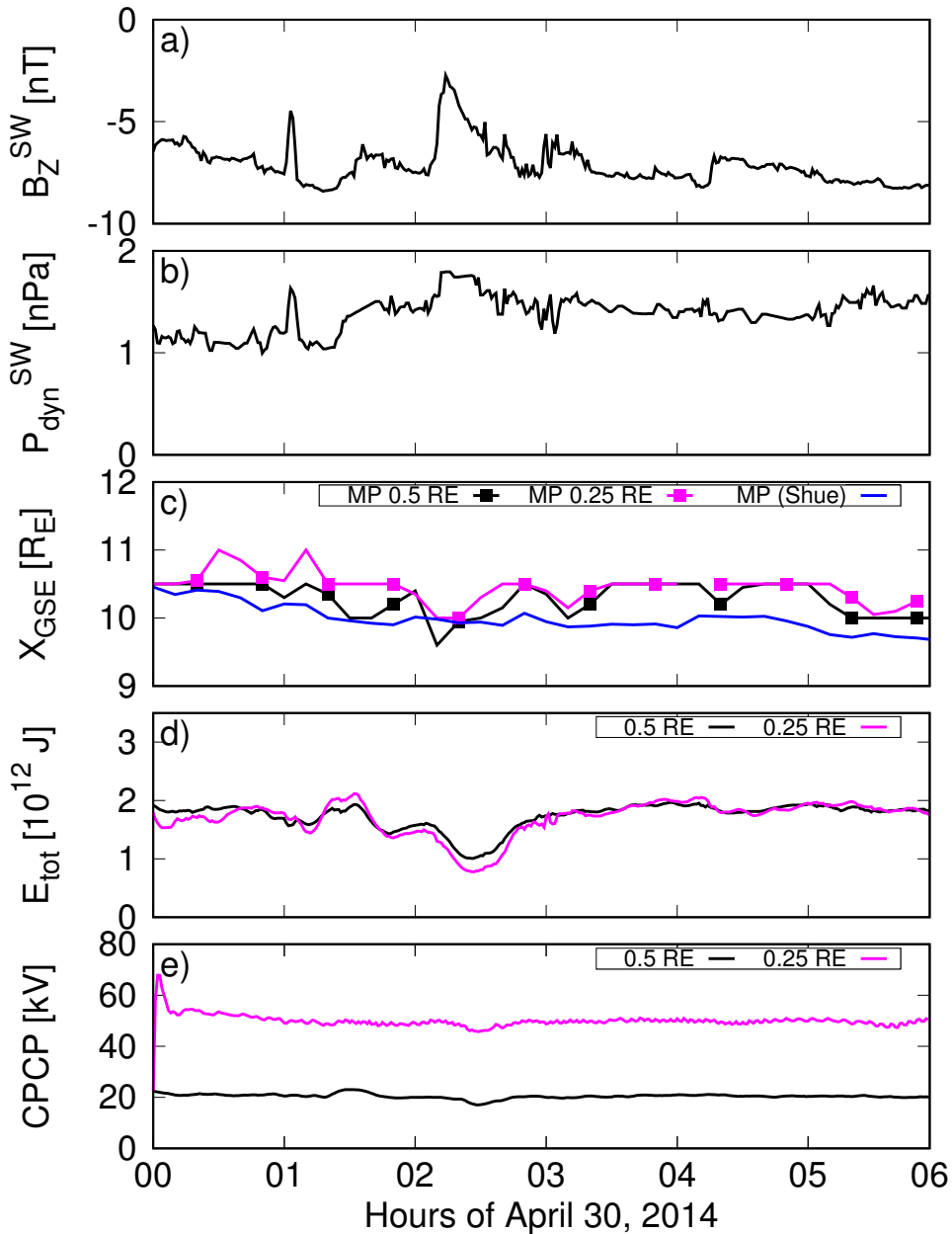
Figure 7. a) Interplanetary magnetic field z component, b) solar wind dynamic pressure, c) the nose of the magnetopause, d) energy transferred from the solar wind into the magnetosphere through the dayside magnetopause, and e) the cross-polar cap potential during April 30 00:00 UT – 06:00 UT, 2014. Black and magenta plots in panels c–d imply which maximum spatial resolution is used (0.5 (black) and 0.25 (magenta) R_E). Blue plot in panel c marks the magnetopause nose computed using the Shue model.
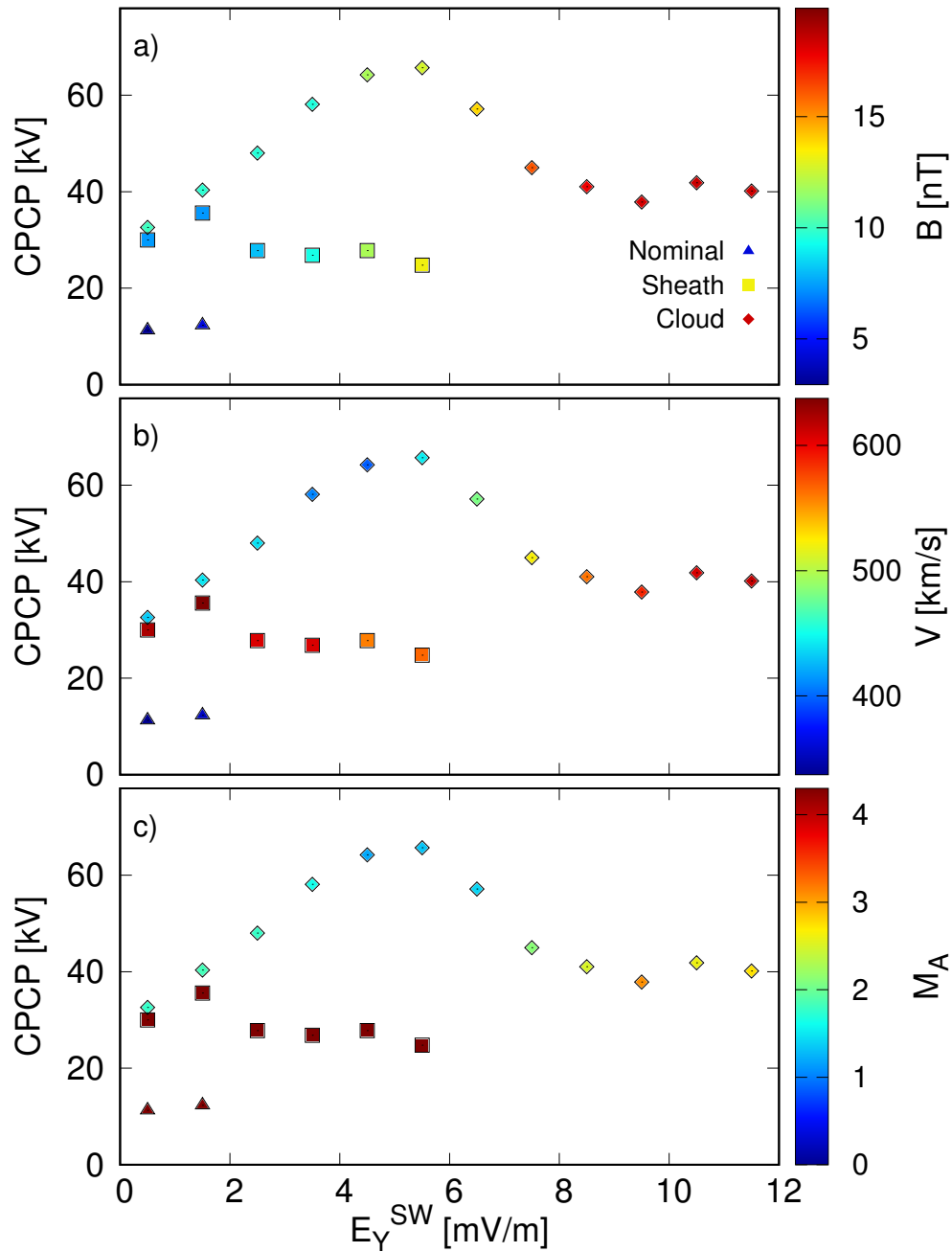
Figure 8. The cross-polar cap potential (CPCP) as a function of the IMF E_Y for the 2012 ICME sheath and cloud periods, with nominal solar wind conditions before and after the ICME event taken into account separately. GUMICS-4 simulation data with 1 minute time resolution has been averaged by 10 minutes and binned by upstream E_Y with 1.0 mV/m intervals. Panels a, b and c are showing the magnitudes of the IMF, the upstream flow speed and the Alfvén Mach number, respectively.
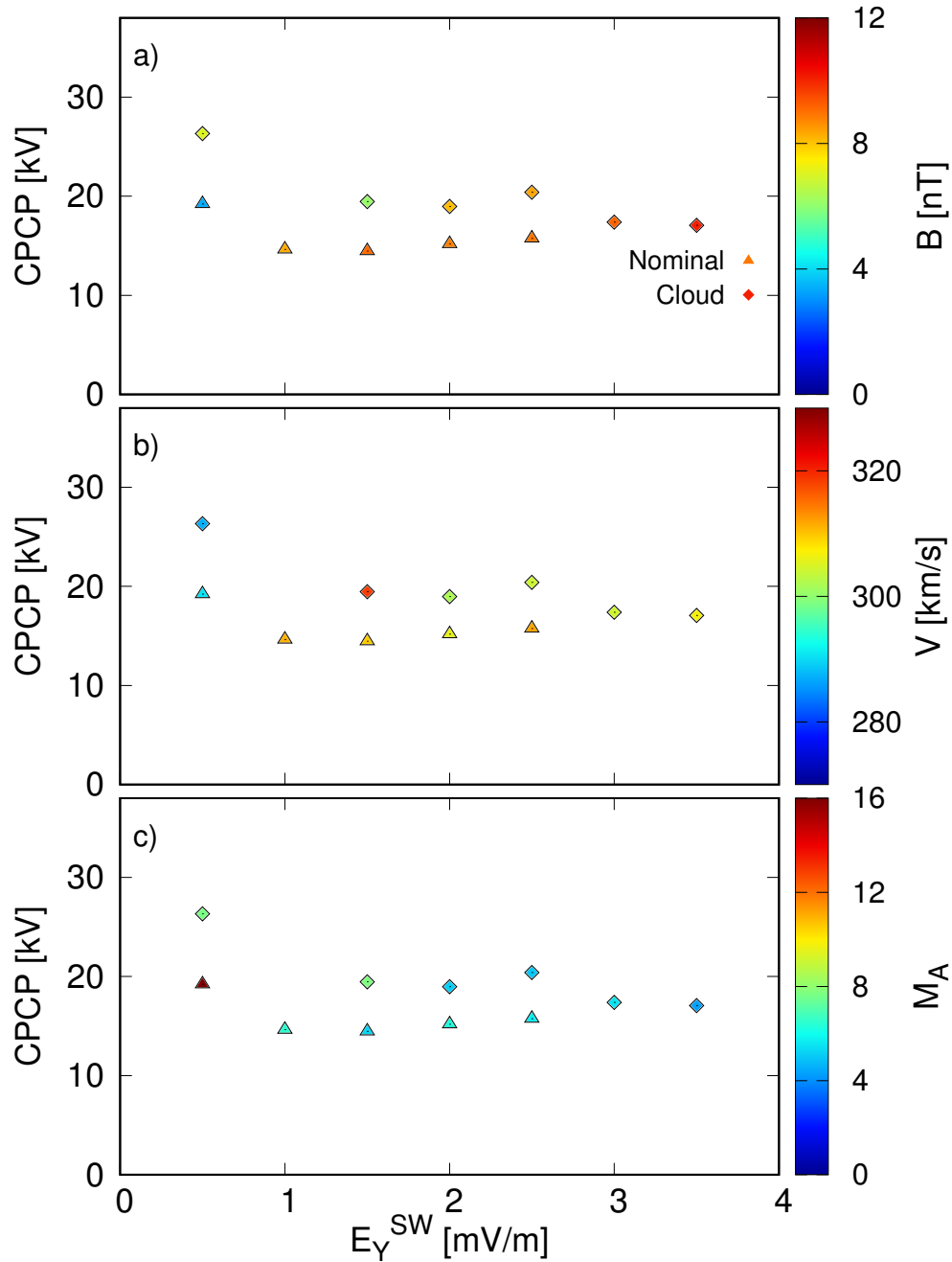
Figure 9. The cross-polar cap potential (CPCP) as a function of the IMF E_Y for the 2014 ICME cloud period, with nominal solar wind conditions before and after the ICME event taken into account separately. GUMICS-4 simulation data with 1 minute time resolution has been averaged by 10 minutes and binned by upstream E_Y with 0.5 mV/m intervals. Panels a, b and c are showing the magnitudes of the IMF, the upstream flow speed and the Alfvén Mach number, respectively.
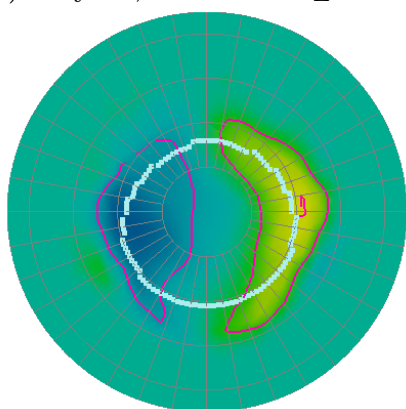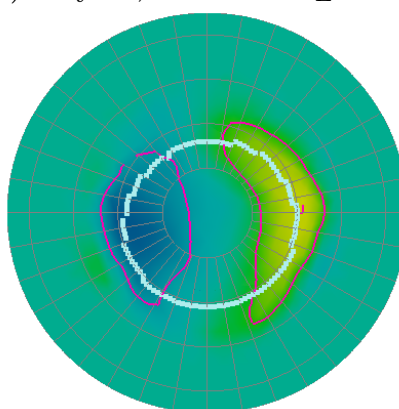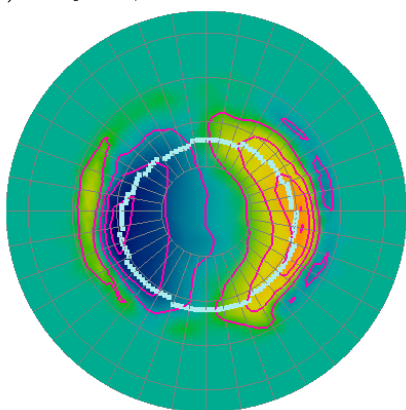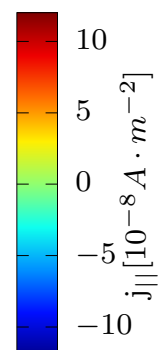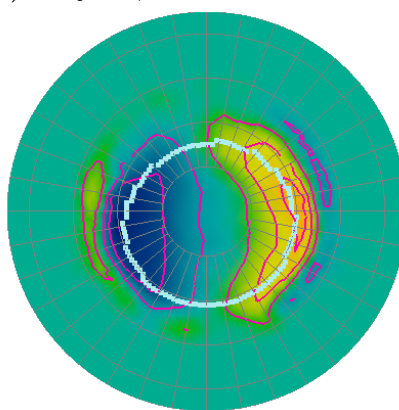
Figure 10. The field-aligned current pattern in GUMICS-4 simulation at 01:00 UT(panels a and c) and at 03:00 UT (panels b and d) in July 16, 2012. Panels a and b (c and d) show the results of the simulation run in which 0.5 (0.25) R_E maximum spatial resolution was used.